PAPER

AORSA full wave calculations of helicon waves in DIII-D and ITER

IOP Publishing | International Atomic Energy Agency Nuclear Fusion

Nucl. Fusion **58** (2018) 066004 (13pp) https://doi.org/10.1088/1741-4326/aab96d

AORSA full wave calculations of helicon waves in DIII-D and ITER

C. Lau[1], E.F. Jaeger[2], N. Bertelli[3], L.A. Berry[2], D.L. Green[1], M. Murakami[1], J.M. Park[1], R.I. Pinsker[4] and R. Prater[4]

[1] Oak Ridge National Laboratory, Oak Ridge, TN, United States of America
[2] XCEL Engineering, Inc., Oak Ridge, TN, United States of America
[3] Princeton Plasma Physics Laboratory, Princeton, NJ, United States of America
[4] General Atomics, San Diego, CA, United States of America

E-mail: lauch@ornl.gov

Received 15 September 2017, revised 6 March 2018
Accepted for publication 26 March 2018
Published 11 April 2018

Abstract

Helicon waves have been recently proposed as an off-axis current drive actuator for DIII-D, FNSF, and DEMO tokamaks. Previous ray tracing modeling using GENRAY predicts strong single pass absorption and current drive in the mid-radius region on DIII-D in high beta tokamak discharges. The full wave code AORSA, which is valid to all order of Larmor radius and can resolve arbitrary ion cyclotron harmonics, has been used to validate the ray tracing technique. If the scrape-off-layer (SOL) is ignored in the modeling, AORSA agrees with GENRAY in both the amplitude and location of driven current for DIII-D and ITER cases. These models also show that helicon current drive can possibly be an efficient current drive actuator for ITER. Previous GENRAY analysis did not include the SOL. AORSA has also been used to extend the simulations to include the SOL and to estimate possible power losses of helicon waves in the SOL. AORSA calculations show that another mode can propagate in the SOL and lead to significant (~10%–20%) SOL losses at high SOL densities. Optimizing the SOL density profile can reduce these SOL losses to a few percent.

Keywords: helicon, current drive, AORSA, electromagnetic simulation, DIII-D, ITER, tokamak

(Some figures may appear in colour only in the online journal)

1. Introduction

For any future magnetic fusion tokamak experiment or reactor such as ITER, FNSF or DEMO to operate in steady state, external non-inductive current drive is necessary to supplement the plasma-generated bootstrap current. The external current must contain both on and off-axis actuators to maintain a weak shear or reversed shear profile for expected high beta H-mode plasmas [1]. Many current drive techniques such as neutral beam current drive (NBCD) [2–6], lower hybrid current drive (LHCD) [7–10], fast wave current drive (FWCD) [11–14], high harmonic fast wave current drive (HHFWCD) [15–17], and electron cyclotron current drive (ECCD) [18–22] have been extensively studied experimentally in various tokamaks and numerically with various simulation tools. This paper focuses on simulations of helicon wave current drive (HCD), which is expected to provide efficient off-axis current drive compared to other alternatives in high beta DIII-D scenarios [23, 24]. Unlike the other techniques, helicon current drive remains untested experimentally, so simulations are necessary to predict current drive efficiency as well as project to reactor relevant tokamaks.

Detailed modeling of the expected HCD was performed using the ray tracing code, GENRAY [25]. For wavelengths smaller than typical scale lengths (minor radius, density gradients), the WKB approximation can be used to reduce Maxwell's equations to a system of ray equations. GENRAY is one such simulation that solves this system of ray equations by calculating the ray trajectories and absorption for a given dispersion relation and a given absorption profile. Because of the reduced computational complexity, GENRAY can be easily used for large parametric scans. In [24], GENRAY simulations showed

that helicon waves can drive significant off-axis current drive that is approximately two times more efficient than NBCD and four times more efficient than conventional ECCD in DIII-D, provided effective coupling of the wave to the plasma can be established. There could be potential issues with the previous GENRAY simulations. The WKB approximation does not allow for diffraction or reflection effects. GENRAY uses a finite Larmor radius expansion that does not calculate ion absorption at high cyclotron harmonics accurately. The ray tracing simulations in [23] and [24] do not include possible scrape-off-layer (SOL) effects and loss mechanisms such as antenna loading [26–28], scattering from fluctuations [29, 30], collisional absorption [31, 32], and parametric decay instabilities [33, 34]. These loss mechanisms could lead to reduced helicon power coupled to the core plasma and reduced helicon current drive efficiency.

To better validate these ray tracing simulations and to account for SOL losses, the massively parallel computing full wave simulation AORSA [35, 36] was used. Like many other hot ion cyclotron full wave codes, AORSA solves a generalization of the Helmholtz equation with the full hot plasma dielectric tensor. AORSA includes diffraction, reflection and mode conversion physics as well as Landau damping and transit time magnetic pumping effects [37]. Unlike other full wave ion cyclotron codes that are valid only to 2nd order or lower order finite Larmor radius and ion cyclotron harmonic number, AORSA is valid to all orders of Larmor radius and can resolve arbitrary ion cyclotron harmonic number. For helicon waves at 30th to 50th ion cyclotron harmonic, this is necessary. AORSA uses the non-relativistic Ehst-Karney parametrization for current drive calculations [38, 39].

In this paper, GENRAY and AORSA results will be shown for DIII-D and ITER cases. Section 2 introduces helicon wave physics, application of helicon wave current drive to DIII-D, and the possible application of helicon wave current drive to ITER. In section 3, AORSA 1D cases are shown to demonstrate that AORSA can numerically resolve the helicon wave in 2D. These simulations also demonstrate that with current computational resources, AORSA 2D can only resolve the helicon wave and not the slow wave. In section 4, AORSA 2D results are shown for DIII-D and ITER for cases where the SOL is not included in the simulation. Comparison to the ray tracing model GENRAY is carried out. For both DIII-D and ITER, good agreement between GENRAY and AORSA 2D is found for current drive and power absorption magnitude and peak radial location. When the SOL is not included in the simulation, the simulated helicon current drive for DIII-D and ITER scenarios can be significantly higher in the mid-radius region compared to other off-axis current drive techniques. In section 5, AORSA 1D and 2D modeling of DIII-D cases with the SOL is described. AORSA 1D modeling is used to show that the slow wave does not appear to have an important effect in helicon wave propagation and absorption. The AORSA 2D cases, however, show a distinct pattern, possibly a standing wave, propagating in the SOL that is not observed in the GENRAY model. Using collisions as a proxy for any physical mechanism that can cause wave dissipation in the SOL, both AORSA 1D and 2D simulations show significant helicon power absorption in the SOL at high SOL densities. Section 6 contains a discussion of the simulation results and their implications for future helicon current drive experiments.

2. Helicon current drive

Helicon waves are fast wave at high ion cyclotron harmonics. The perpendicular index of refraction, $n_\perp$, of the helicon wave is shown in equation (1) as a function of plasma parameters and parallel index of refraction, $n_{||}$. S and D are cold plasma Stix parameters [40]. ε_{33} is the component of the warm Maxwellian dielectric tensor parallel to the magnetic field and is defined to be $2\xi_e^2[1+\xi_e Z(\xi_e)]$ where ξ_e is the ratio of the parallel phase velocity to the electron thermal velocity, and $Z(\xi_e)$ is the plasma dispersion function [40].

$$n_\perp = \sqrt{\frac{(S - n_{||}^2)^2 - D^2}{S - n_{||}^2 + D^2 \frac{\mathrm{Re}(\varepsilon_{33})}{|\varepsilon_{33}|^2} \frac{n_{||}^2}{(S-n_{||}^2)}}}. \quad (1)$$

The imaginary component of the perpendicular index of refraction, $n_{\perp i}$, is shown in equation (2) where β_e is the electron beta, ω_{pe} is the electron plasma frequency, ω_{ce} is the electron cyclotron frequency, and G is a dimensionless term that depends on many non-dimensional plasma parameters. The full description of G is shown in [24]. The single pass absorption rate, A, is shown in equation (3). A depends on $n_{\perp i}$ and is a useful metric for helicon wave absorption efficiency.

$$n_{\perp i} = \frac{\sqrt{\pi}}{4} n_\perp \beta_e \xi_e e^{-\xi^2} G\left(n_{||},\ S,\ D,\ \varepsilon_{33},\ \frac{\omega_{pe}}{\omega_{ce}},\ \frac{kT_e}{mc^2}\right) \quad (2)$$

$$A = 1 - 2\int_{-\infty}^{\infty} \frac{\omega}{c} n_{\perp i} \mathrm{d}l. \quad (3)$$

As discussed in detail in [24], equation (1) can be used to understand wave propagation in tokamaks given that $n_\parallel$ is largely set by the antenna. For DIII-D parameters, helicon waves propagate close to magnetic field lines with a small radial component. Equations (2) and (3) can be used to understand wave absorption for helicon waves and their application to current drive in tokamaks. With sufficiently high single pass absorption and strong damping, the wave will damp and drive current off-axis. For high beta DIII-D discharges, GENRAY parametric scans of antenna location, frequency, and $n_\parallel$ indicate that strong absorption by electron Landau damping can be obtained at ~500 MHz, $n_\parallel = 3$, and antenna above the midplane. The results are not very sensitive to $n_\parallel$, so $n_\parallel$ was chosen by antenna loading and accessibility considerations. If $n_\parallel$ is large, antenna loading becomes small because the helicon fast wave needs to tunnel through an evanescence layer. The attenuation of the helicon fast wave through this evanescence layer depends strongly on $n_\parallel$. If $n_\parallel$ is small, the helicon fast wave can mode convert to a slow wave, preventing the helicon fast wave from accessing the plasma core. Launching helicon waves above the midplane produced slightly better results and allowed for easier port access on DIII-D. The choice of frequency is critical as a balance between accessibility considerations and undesired fast ion damping from neutral beams.

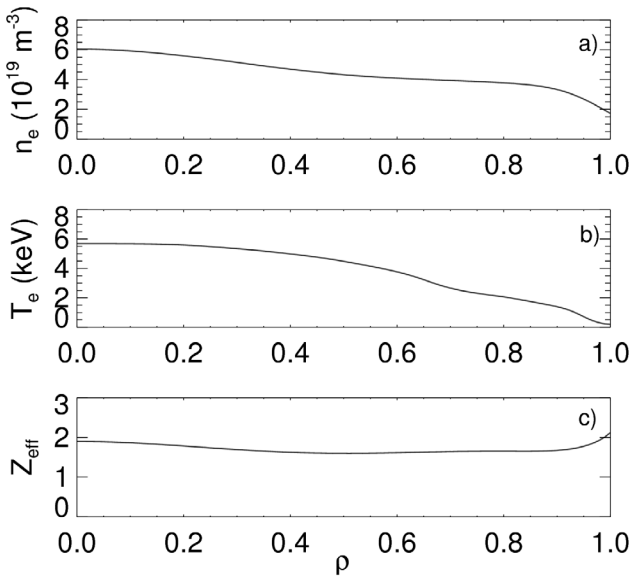

Figure 1. (*a*)–(*c*) The electron density, temperature, and $Z_{\rm eff}$ is shown for the DIII-D scenario, respectively as a function of the square root of the normalized toroidal flux, ρ.

The predicted large mid-radius helicon current drive in [24] has led to recent low power tests of helicon antenna loading [27, 28]. Success of these low power experiments have led to plans for high power experiments on DIII-D. Development of a high power helicon system [41] and a new travelling wave antenna [42] to deliver 1 MW of helicon power at 476 MHz to the DIII-D tokamak is in progress. 476 MHz is chosen because it is close to the chosen 500 MHz from the GENRAY parametric scans and because of the availability of 1.2 MW, 476 MHz klystron systems from the Stanford Linear Accelerator to provide power to the antenna. The travelling wave antenna is a 30-module system where the input power is fed on the side of the antenna, travels toroidally through the 30 modules, and outputs on the other side of the antenna at another toroidal location. It is located above the midplane and optimized to an expected center $n_{\|}$ value of 3. The width of the vacuum $n_{\|}$ spectrum is expected to be narrow because of the large number of modules. Some spectrum modification may be possible due to plasma effects.

The DIII-D scenario chosen for this paper is from an integrated modelling effort using the FASTRAN code [43] in 2012 to guide potential upgrades to heating and current drive systems. The scenario assumes $B_0 = 1.75$ T, $I_{\rm p} = 2$ MA, 9 MW of ECCD power to provide current drive as far off-axis as possible. 14 MW of neutral beam power is also deposited off-axis, so that the current profile has weak magnetic shear and a beta of about 5% [43, 44]. The electron density, temperature, and $Z_{\rm eff}$ is shown in figure 1 as a function of the square root of the normalized toroidal flux, ρ. The density peaks at 6×10^{19} m^{-3} and almost 6 keV in the core. With upgrades to ECH and neutral beam power, this scenario is envisioned as a possible future high beta, fully non-inductive DIII-D discharge. Helicon simulations for this scenario assumes 476 MHz frequency and 1 MW coupled input power to the plasma. 1 MW is chosen because of the estimated transmission line and coupling losses from the 1.2 MW sources. The

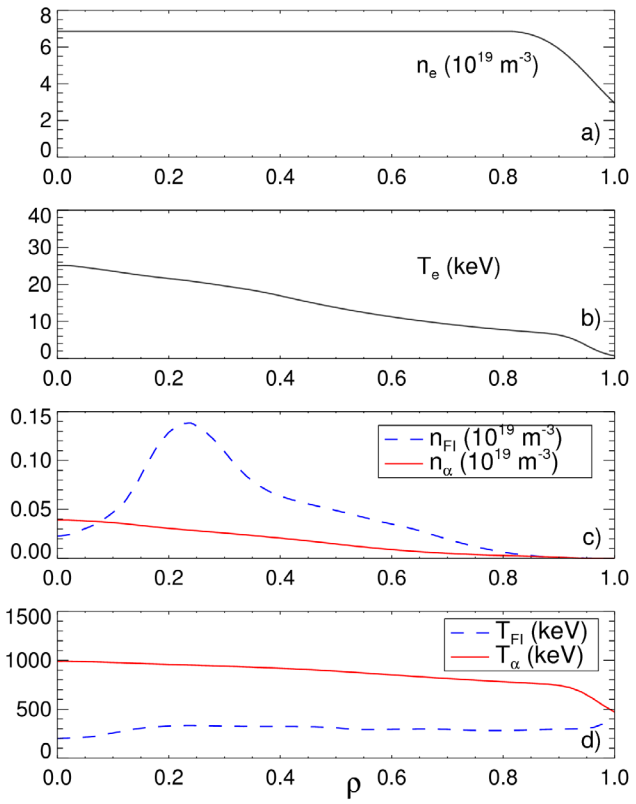

Figure 2. (*a*) Electron density (*b*) electron temperature (*c*) fast ion (blue dashed line) and alpha density (red solid line) (*d*) fast ion (blue dashed line) and alpha (red solid line) temperature is shown for the ITER scenario.

equations that GENRAY and AORSA solve are linear, so the total current driven scales linearly with the absorbed power and the simulations can be scaled appropriately if the coupled power is different than expected.

An integrated ITER scenario [45] was also chosen for this paper to show the possibility of helicon current drive in a burning plasma experiment. The electron density and temperature profiles are shown in figures 2(*a*)) and (*b*)). The fast ion and alpha density are shown in figure 2(*c*)) and the fast ion and alpha temperature are shown in figure 2(*d*)). The density is approximately 7×10^{19} m^{-3} with equal deuterium and tritium ion ratio density. Core temperature is ~25 keV and $Z_{\rm eff}$ is assumed to be equal to 2 throughout the core plasma. This is a weak magnetic shear scenario optimized using the GLF23 transport model and benchmarked by other models, such as the FASTRAN model. The scenario assumes 33 MW of neutral beam power, 20 MW of electron cyclotron power, and 20 MW of ion cyclotron power in a $B_0 = 5.3$ T, $I_{\rm p} =$ 8 MA discharge. Fast deuterium ions from the 1 MeV neutral beam is calculated from the NUBEAM code [46]. Alphas from the D–T reaction are also calculated from NUBEAM using the Bosch–Hale cross sections. The calculated density and temperature from NUBEAM is for a stationary equilibrium distribution where the alphas and fast ions slow down to thermal plasma temperatures. Depending on the choice of frequency, the fast ions and alphas may be important. 1 MW input power and $n_{\|} = 3$ is assumed for the AORSA simulations. This is shown in section 4.

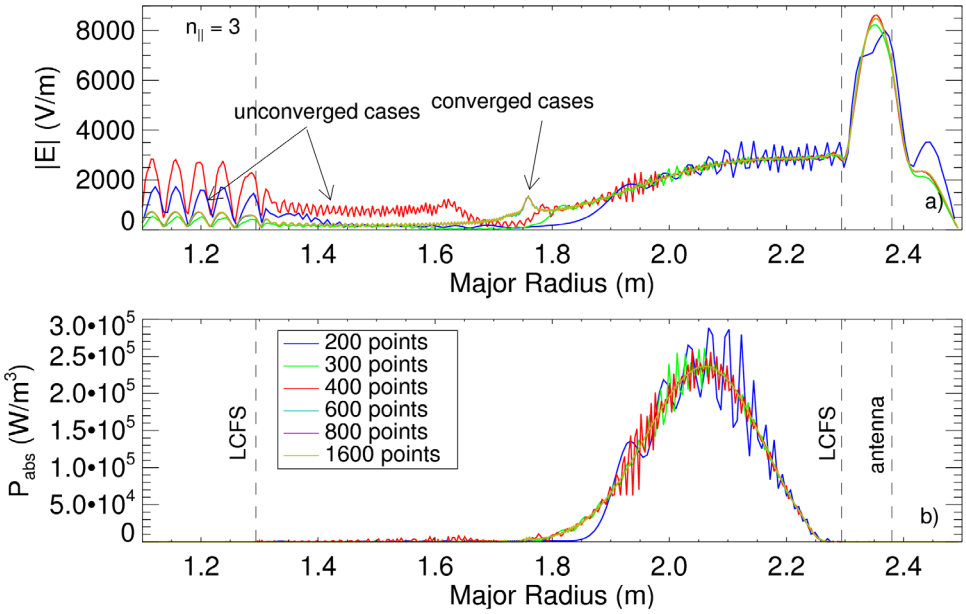

Figure 3. AORSA 1D simulation of DIII-D integrated scenario at $n_{\|} = 3$. (*a*) $|E|$ for various grid points. (*b*) P_{abs} for various grid resolutions.

In later sections, GENRAY and AORSA calculations show that there can be 100% single pass absorption and large mid-radius current drive for the plasma scenarios chosen in this paper. Estimates of the single pass absorption rate for various DIII-D parameters are shown in [24].

For this paper, the convention is that $n_{\|}$ is positive when the toroidal field is clockwise from the top of the torus. DIII-D can operate the toroidal field for both clockwise and counter-clockwise direction, and the DIII-D antenna is designed to launch the helicon wave in either positive or negative $n_{\|}$ for scenarios with either toroidal field direction and either co- or counter-current drive direction.

3. AORSA 1D simulations for DIII-D

The AORSA simulations were obtained on the supercomputing clusters located at the National Energy Research Scientific Computer center (NERSC). For the results of this paper, AORSA is solved in both one dimension (1D) in the radial direction and two dimensions (2D) in the radial and vertical directions. Due to the high frequency and short wavelengths of helicon waves (~500 MHz) compared to typical fast waves, the AORSA 2D helicon wave simulations are computationally intensive and require significantly more computational resources than typical AORSA 2D fast wave simulations. The AORSA 2D results used ~300–600 grid points in both the radial and vertical dimensions. This is within the capabilities of the estimated maximum 600 × 600 grid points for AORSA 2D simulation with the current computational resources on NERSC. A convergence scan using up to 1600 grid points in AORSA 1D simulations indicates that ~300–600 grid points for AORSA 1D and 2D are sufficient to resolve the helicon wave. AORSA 1D simulations also have enough grid points to resolve the slow wave in the SOL, which is currently not possible in the AORSA 2D simulations.

The AORSA 1D electric field, $|E|$, and power absorbed on the electrons, P_{abs}, for $n_{\|} = 3$ are shown for 200, 300, 400, 600, 800, and 1600 radial grid points in figures 3(*a*) and (*b*) for the above-mentioned DIII-D scenario, respectively. It can be seen in figure 3 that 200 (blue), 300 (green), and 400 (red) points give different solutions than the 600 (cyan), 800 (purple), and 1600 (yellow) points. This is especially noticeable in the $|E|$ in the inner SOL. 600, 800, and 1600 points give similar answers for helicon $|E|$ field and P_{abs}, indicating that the solution has converged and that 600 points is sufficient for an accurate calculation.

Similarly, the AORSA 1D electric field, $|E|$, and P_{abs}, for $n_{\|} = 4$ is shown for 200, 300, 400, 600, 800, and 1600 grid points in figures 4(*a*) and (*b*), respectively. In this case, only 200 and perhaps 300 grid points appear to give a substantially different solution for $|E|$. 300–400 grid points appear sufficient for an accurate calculation. The minimum number of grid points can be estimated by calculating the perpendicular helicon wavelength from the dispersion relation in equation (1). The perpendicular wavelength of the helicon fast wave is shown in figure 5 for both the $n_{\|} = 3$ (blue) and $n_{\|} = 4$ (red) case. From Nyquist's theorem, a minimum of at least 2 grid points per wavelength is needed to resolve the solution. For a 1.4 m radial grid and minimum 0.8 cm to 1.1 cm helicon wavelength for the $n_{\|} = 3$ and $n_{\|} = 4$ cases, 2 grid points per wavelength gives an estimated minimum of 250–375 grid points to resolve the helicon wave. Based on the 1D AORSA solutions, it appears that ~3–4 grid points per wavelength (~300–600 grid points) is sufficient for a converged solution. In all the subsequent 2D AORSA simulations, 300–600 grid points are used in both the radial and poloidal dimension. The exact number of grid points differ depending on the case. For higher densities, higher frequency, and lower $n_{\|}$, equation (1) can be used to show that the perpendicular refractive index is larger, so the perpendicular wavelength is smaller and a finer grid resolution is necessary.

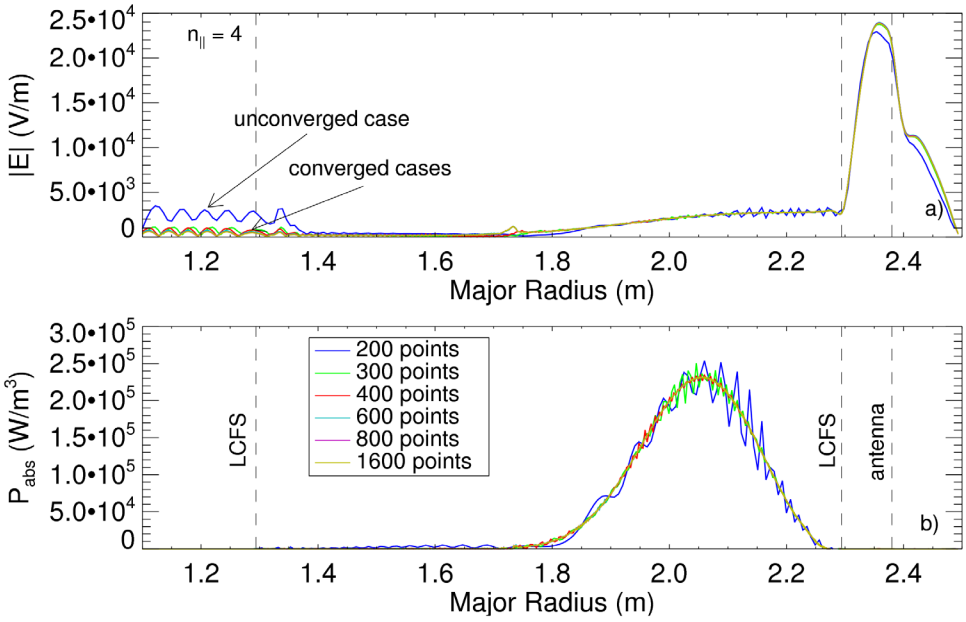

Figure 4. AORSA 1D simulation of DIII-D integrated scenario at $n_{\|} = 4$. (*a*) $|E|$ for various grid points. (*b*) $P_{\rm abs}$ for various grid points.

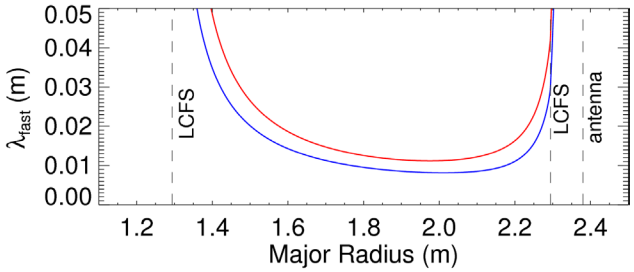

Figure 5. Helicon fast wave dispersion relation for $n_{\|} = 3$ (blue) and $n_{\|} = 4$ (red) for the DIII-D integrated scenario.

4. Comparison between AORSA 2D and GENRAY for DIII-D and ITER without SOL

For the AORSA 2D simulations, recent computational upgrades to AORSA have allowed for converged helicon mode calculations by reducing the numerical pollution of AORSA results [47]. AORSA had been susceptible to numerical noise for cases with strong electron Landau damping. The numerical noise increases with higher mesh resolution. Helicon waves require a large mesh resolution since they have relatively short wavelengths compared to typical waves used for ICRF heating. Electron Landau damping is also the dominant damping mechanism for helicon waves, so reducing numerical pollution is essential. In [47], a new plasma dispersion function has been developed to account for the fact that the local wave vector cannot be assumed to be a straight magnetic field line, and that is in fact curved. This assumption is especially problematic for the case of electron Landau damping. The new plasma dispersion function allows for resonance broadening of $k_{\|}$ from electron motion in curved magnetic field lines. This not only includes more accurate physics for electron Landau damping but is also used to reduce the numerical pollution of strong electron Landau damping cases. To be consistent with the new plasma dispersion function, the power absorbed ('Wdot' or dW/dt) now includes dissipative and non-dissipative terms. Wdot is used for the calculation of power absorption and current drive efficiency. Full details of these numerical upgrades are in [47].

The GENRAY calculations shown in this paper used the cold plasma dispersion relation, a single ray, and an ion absorption model derived for high harmonic fast waves [48]. The non-relativistic Ehst–Karney formula is used for current drive. Previous work [24] using GENRAY has shown that the power absorption and current drive are surprisingly insensitive to the number of rays, choice of either cold or hot plasma dispersion relation, or different ion absorption models. The simplest GENRAY results are therefore used in this paper to compare with the AORSA results. A Maxwellian distribution for the electron distribution function is assumed in this paper. Electron Landau damping from high power waves can modify the electron distribution function. The use of a Fokker–Planck model, such as CQL3D [49], to account for non-Maxwellian populations was done previously in [24] and showed that CQL3D only minimally modifies the electron distribution function and current drive profile for the cases calculated in this paper. Given this initial result and noting that iteration between AORSA and CQL3D adds additional numerical complexity, non-Maxwellian distributions are considered outside the scope of this paper.

Multiple comparisons between GENRAY and AORSA are chosen for both DIII-D and ITER discharges. These comparisons were chosen for both numerical and physics reasons. The main physics goal of the AORSA simulations of DIII-D discharges is to compare GENRAY and AORSA to validate the choice of antenna parameters chosen, such as antenna $n_{\|}$, frequency, and locations in [24]. Antenna locations on the mid-plane and above the mid-plane were chosen, and $n_{\|} = 3$ and 4 were chosen to match those in [24]. AORSA simulations are computationally intensive and some simulations were not possible for the desired antenna parameters. Some

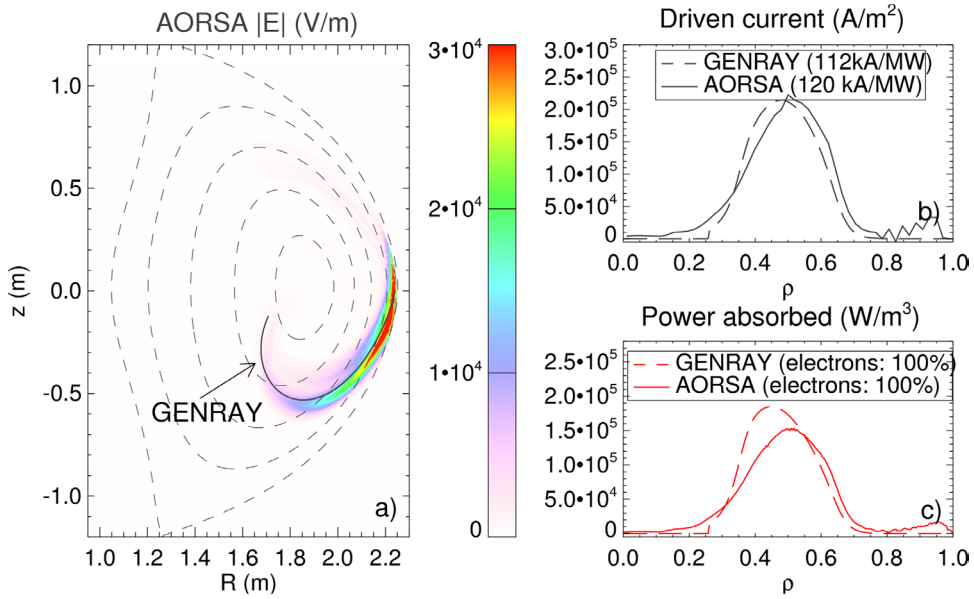

Figure 6. (*a*) AORSA |*E*| (colors) and GENRAY ray (black line) for DIII-D integrated scenario at frequency of 476 MHz and $n_{||} = 3$. (*b*) Flux surface integrated driven current. (*c*) Flux surface integrated power absorbed.

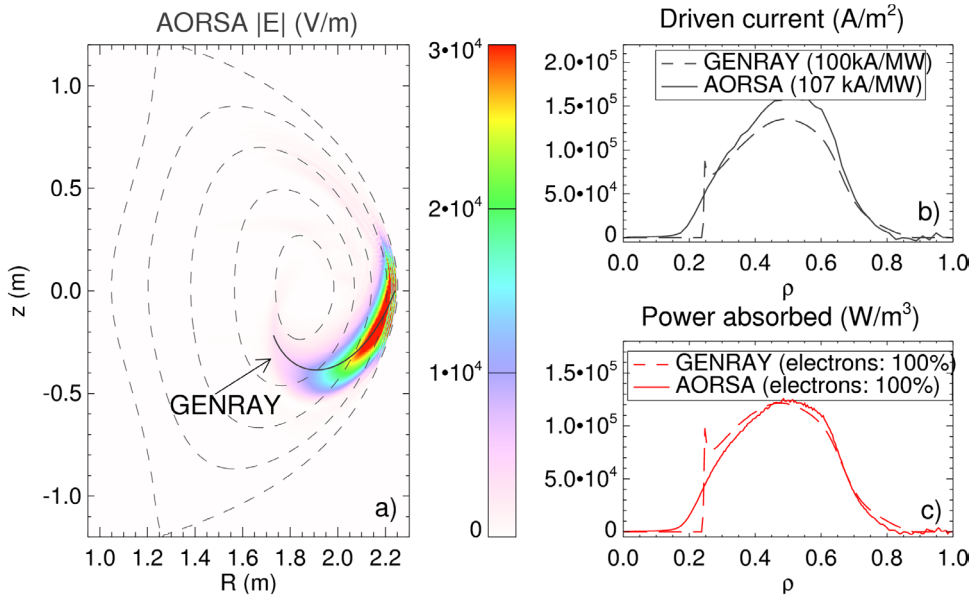

Figure 7. (*a*) AORSA |*E*| (colors) and GENRAY ray (black line) for DIII-D integrated scenario at frequency of 476 MHz and $n_{||} = 4$. (*b*) Flux surface integrated driven current. (*c*) Flux surface integrated power absorbed.

of the converged AORSA simulations cases are shown here. For all converged AORSA simulations for the DIII-D scenario without the SOL that have been achieved to date, there is good agreement with the GENRAY results. Further comparisons between GENRAY and AORSA for the ITER discharges also showed good agreement if electron Landau damping is the dominant absorption mechanism.

The 2D electric field profiles are shown in figure 6(*a*)) for the DIII-D scenario. The black dashed lines are contours of the normalized flux, ρ, at 0.2, 0.4, 0.6, 0.8, and 1. The GENRAY ray trajectory is also shown by the black solid line in figure 6(*a*)). The GENRAY result agrees with the shape of the AORSA 2D electric field profiles. To further quantify the comparison between AORSA and GENRAY, the AORSA 2D power absorption and driven current profiles for $n_{||} = 3$ are flux surface integrated and plotted in the solid lines in figures 6(*b*) and (*c*). The GENRAY power absorption and current driven along the ray is flux surface mapped to ρ and shown by the dashed lines in figures 6(*b*) and (*c*). The power absorption for both simulations is dominated by electron Landau damping (>99% absorption to the electron channel). The power absorption also peaks in the mid-radius region ($.4 < \rho < .6$). The AORSA profiles are slightly broader than GENRAY, but the total current predicted by AORSA is only ~5%–10% higher than GENRAY for this case and for all the cases shown below in this section.

Similar results for $n_{||} = 4$ cases are shown in figures 7 and 8 for helicon waves launched at the midplane and above

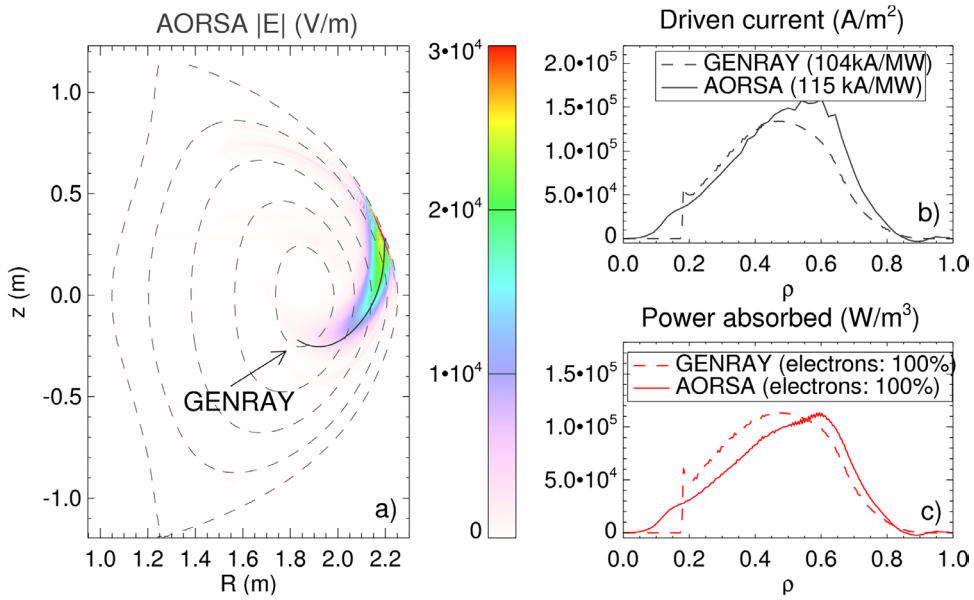

Figure 8. (*a*) AORSA |*E*| (colors) and GENRAY ray (black line) for DIII-D integrated scenario at frequency of 476 MHz, $n_{\|} = 4$, and above the midplane helicon launch. (*b*) Flux surface integrated driven current. (*c*) Flux surface integrated power absorbed.

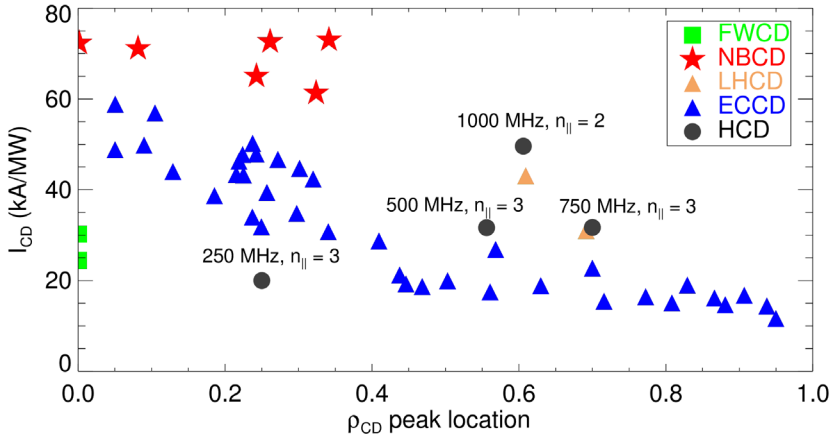

Figure 9. Calculation of current drive amplitude and location for ITER steady state scenario. For the HCD cases, the GENRAY calculations for the current drive efficiency are plotted. The AORSA calculations for 500 and 750 MHz are 10%–15% higher than the GENRAY and suggest even better HCD efficiency.

the midplane. AORSA electric field profiles, flux surface integrated driven current, and flux surface integrated power absorption are shown in figures 7(*a*)–(*c*) for the midplane case, respectively. AORSA electric field profiles, flux surface integrated driven current, and flux surface integrated power absorption are shown in figures 8(*a*)–(*c*) for the above the midplane case, respectively. The agreement between the GENRAY ray trajectories and AORSA |*E*| fields is good for both of these cases. The magnitude and peak radial location of the helicon current drive and power absorption also are in good agreement for both cases.

To further evaluate possible differences between GENRAY and AORSA and to understand the possible utility of HCD on ITER, GENRAY and AORSA simulations were carried out for the chosen ITER scenario. Figure 9 shows the previous results for ECCD (blue triangles), NBCD (red stars), FWCD (green squares), LHCD (brown triangles) from figure 7 of [45] as well as the newly calculated HCD (black circles) for different helicon frequencies and $n_{\|}$ studied. As shown in figure 9, the use of 1 GHz helicon wave with a $n_{\|} = 2$ could be an attractive option for driving current in the mid-radius region. HCD efficiency at 1 GHz and $n_{\|} = 2$ is a factor of 2 to 3 greater than ECCD and approximately 15% greater than LHCD.

For three of these cases, the current drive location and amplitude are calculated with AORSA. Unfortunately, the memory limitations of AORSA on the NERSC supercomputer precluded its use for the highest frequency case at 1 GHz and $n_{\|} = 2$. Lower frequency cases, however, could be simulated using AORSA. Comparison of GENRAY versus AORSA for three cases are shown below for 250 MHz, 500 MHz, and 750 MHz in figures 10–12.

When the frequency is 250 and 500 MHz, the GENRAY trajectory matches the AORSA electric fields. Both codes predict similar current drive profiles in terms of magnitude and peak location. Significant power loss to the fast alpha and deuterium beam ions is predicted by both codes. There are

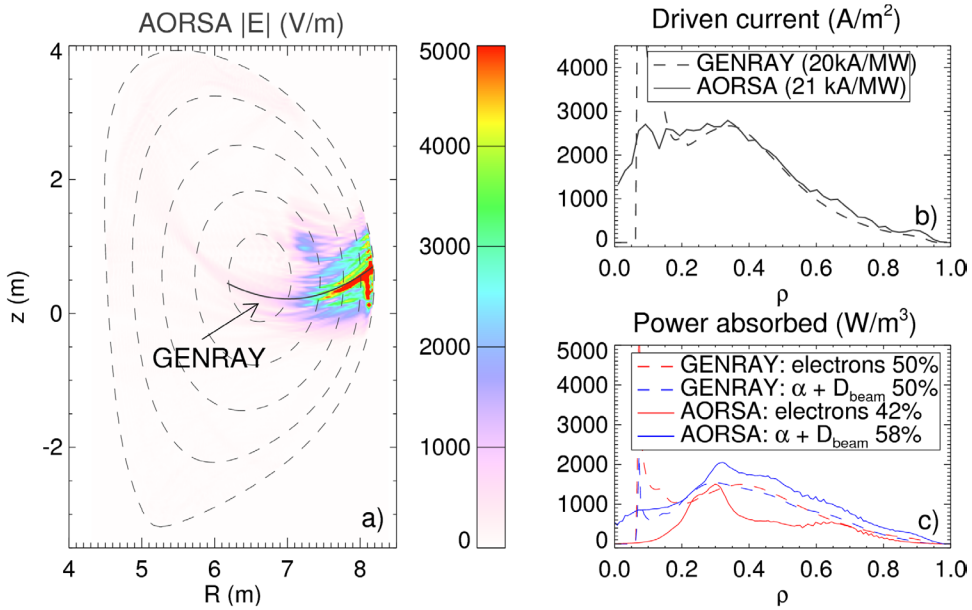

Figure 10. (*a*) AORSA |*E*| and GENRAY ray for ITER integrated scenario at frequency of 250 MHz and $n_{||} = 3$. (*b*) Flux surface integrated driven current. (*c*) Flux surface integrated power absorbed.

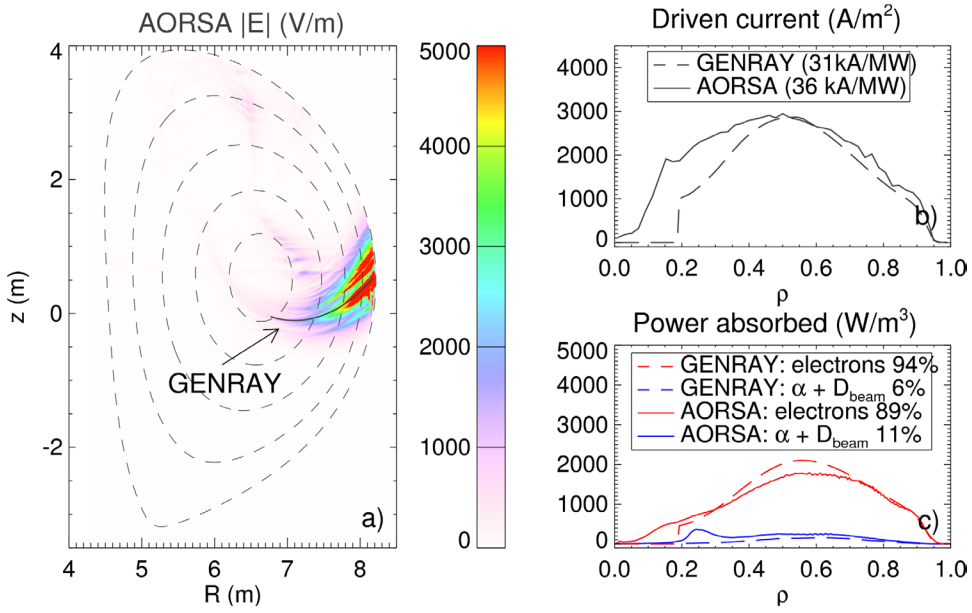

Figure 11. (*a*) AORSA |*E*| and GENRAY ray for DIII-D integrated scenario at frequency of 500 MHz and $n_{||} = 3$. (*b*) Flux surface integrated driven current. (*c*) Flux surface integrated power absorbed.

some differences between the two codes. There does appear to be some difference between the proportion and location of the helicon power transferred to the bulk electrons versus fast ions and beam ions in the two codes. For comparison between GENRAY and AORSA, this should not be too important because the helicon frequency should be chosen to be high enough to avoid strong fast ion and beam ion losses. Any frequency chosen for current drive will therefore have minimal fast ion and beam ion losses and minimal differences in these losses between codes. At 750 MHz, the power is predominantly absorbed by the electrons, similar to the DIII-D case. The agreement between the two codes is also good in this case for current drive and power deposition magnitude and location.

5. AORSA and GENRAY modeling for DIII-D with SOL

While the agreement between GENRAY and AORSA is good for many cases, the above simulations do not take the SOL into account. The antenna is necessarily located in the cold SOL, where there could be other significant physical mechanisms such as plasma-antenna loading, parametric decay instabilities, scattering from fluctuations, slow waves, and electron-neutral collisions. It is therefore necessary to investigate these possible SOL mechanisms and identify possible SOL loss channels. RF power losses in the SOL near this frequency range have been observed experimentally for LH waves on many experiments [50] and high harmonic fast

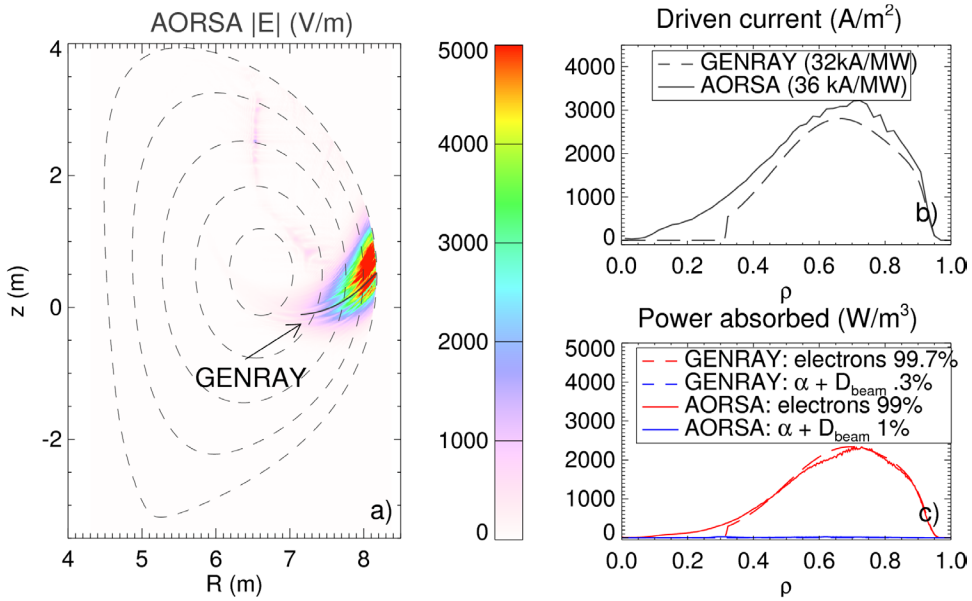

Figure 12. (*a*) AORSA |*E*| and GENRAY ray for ITER integrated scenario at frequency of 750 MHz and $n_{\|} = 3$. (*b*) Flux surface integrated driven current. (*c*) Flux surface integrated power absorbed.

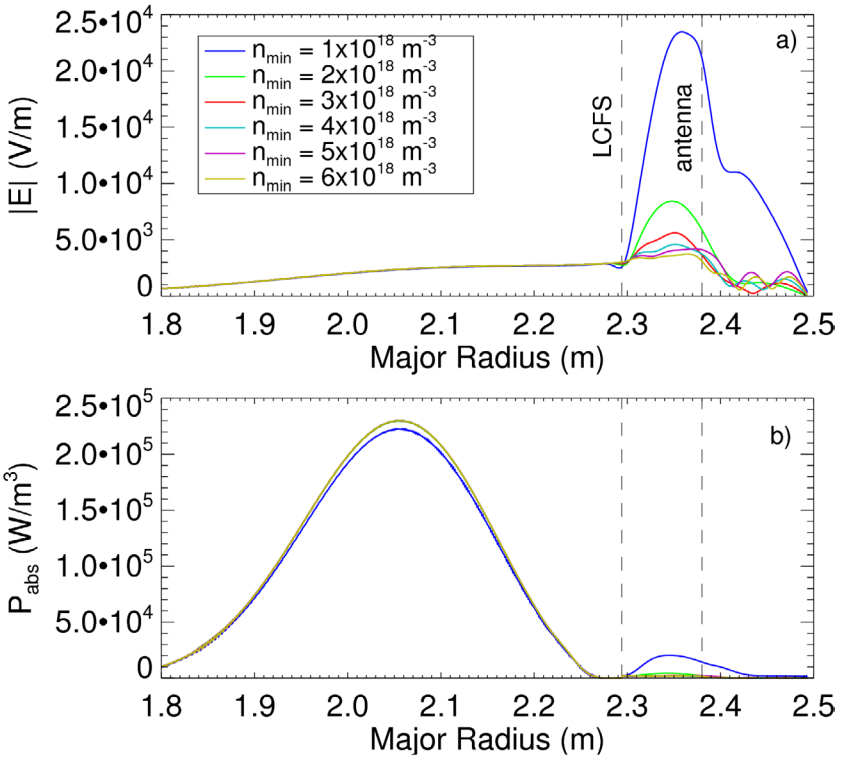

Figure 13. AORSA 1D solution for DIII-D case including the SOL. (*a*) |*E*| for various $n_{\min}$. (*b*) P_{abs} for various $n_{\min}$.

waves on NSTX [51]. To investigate possible SOL loss mechanisms, this paper follows the numerical approach outlined in previous papers using AORSA to study SOL losses [52, 53]. The SOL density profile is modelled as a radial exponential decay, shown in equation (4) below where $n_{\min}$ and L are the minimum electron density in front of the antenna and the SOL decay length, respectively. Both these parameters are inputs to the AORSA model that can be varied, so as to study the sensitivity of the helicon current drive efficiency to the details of the SOL density profile.

$$n_{\text{e}} = n_{\min} + [(n_{\text{e}}(\rho = 1) - n_{\min}] * e^{-\frac{\rho - 1}{L}}. \quad (4)$$

Estimates of the SOL losses is achieved using a collisional frequency, ν, that is implemented by replacing the mass with an effective mass that includes an imaginary term [40]. ν is also an input parameter to AORSA. If $\nu = 0$, no significant power absorption is observed in the SOL. ν is therefore a proxy for possible physical mechanisms and allows for study of SOL losses as a function of SOL density. At the moment,

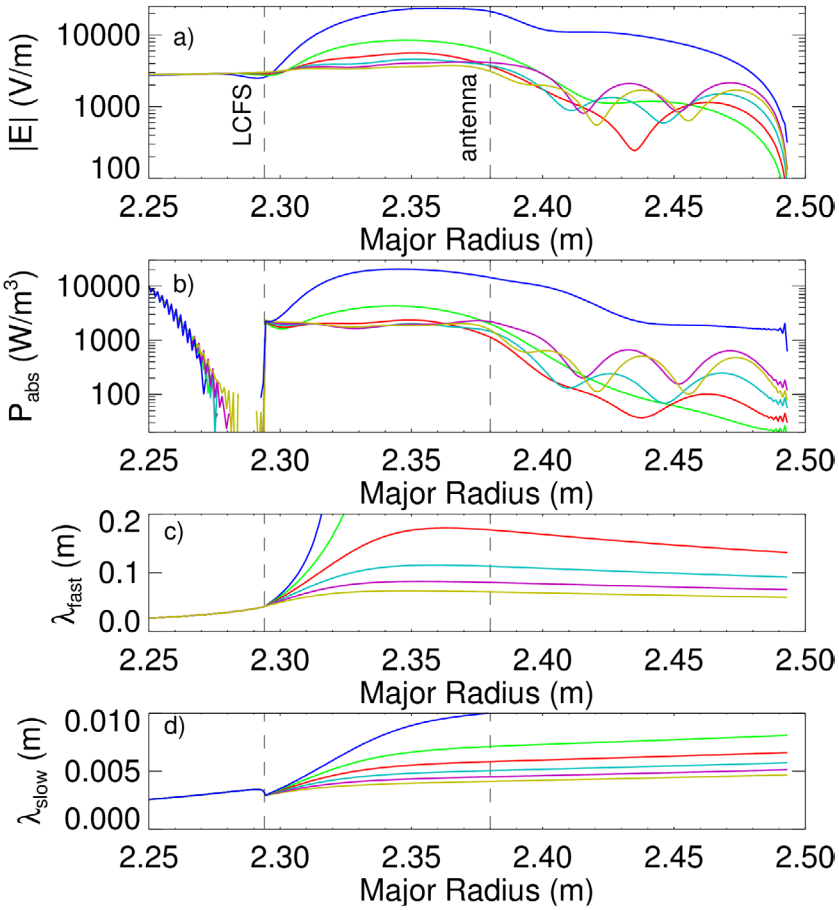

Figure 14. A close-up of figure 13 for the radial region containing the outer SOL. (*a*) |*E*| for various $n_{\min}$. (*b*) P_{abs} for various $n_{\min}$. (*c*) Helicon fast wave perpendicular wavelength for various $n_{\min}$. (*d*) Slow wave perpendicular wavelength for various $n_{\min}$.

there is a lack of quantitative understanding of all the physical mechanisms for helicon power absorption in the SOL. To illustrate the importance of the SOL density on the power losses in the SOL, ν/ω is therefore chosen to equal .01 in this paper. This has previously been used in AORSA simulations [52] where it is shown that the power lost to the SOL increases with increasing ν/ω for AORSA calculations of NSTX conditions. The estimates and conclusions in this section are therefore qualitative and are used to understand trends in the SOL losses as a function of SOL density. The quantitative calculated loss requires better understanding of SOL density profiles and physical loss mechanisms.

Both AORSA 1D and 2D simulations are used to model helicon power loss in the SOL. Starting with AORSA 1D, the |*E*| and P_{abs} profile as a function of the major radius are shown for various $n_{\min}$ in figures 13(*a*) and (*b*), respectively. The number of radial grid points used is 1600. Based on calculations of the fast and slow wave perpendicular wavenumber from the dispersion relation, 1600 grid points is sufficient to resolve the fast wave throughout the simulation and both the fast and slow waves in the SOL. The |*E*| of the helicon wave in the core plasma are almost identical for all cases. There is a slightly lower core P_{abs} in the $n_{\min} = 1 \times 10^{18}$ m^{-3} case. Unlike the solution in the core, the solution in the SOL is very different for all 7 cases. A close-up of these 7 cases in figure 13 within the SOL is shown in figures 14(*a*) and (*b*). Figures 14(*c*)) and

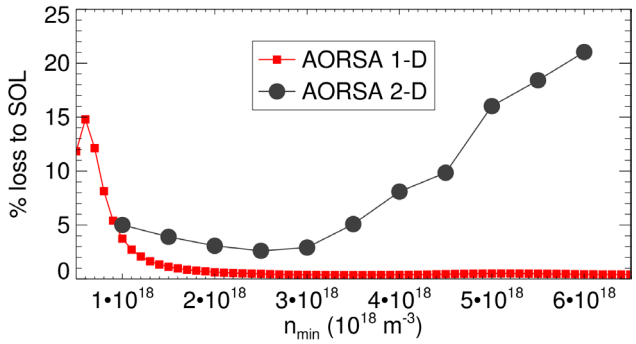

Figure 15. Fractional power loss to the SOL for AORSA 1D simulations.

(*d*) also show the perpendicular wavelength for the helicon fast wave and slow wave. For all the cases, the |*E*| field peaks radially inwards of the antenna. For $n_{\min} \leqslant 2 \times 10^{18}$ m^{-3} where the helicon fast wave is evanescent for at least parts of the SOL, the |*E*| field decays away from the peak location. Behind the antenna, for $n_{\min} \geqslant 3 \times 10^{18}$ m^{-3} where the helicon fast wave is propagating in the SOL, the |*E*| field oscillates in the SOL with wavelength on the order of a few cm. The wavelength of these oscillations is shorter for higher densities and is approximately half of the expected fast wave perpendicular wavelength (~few cm) at those densities. While the grid resolution is high enough to resolve the slow wave, no oscillations

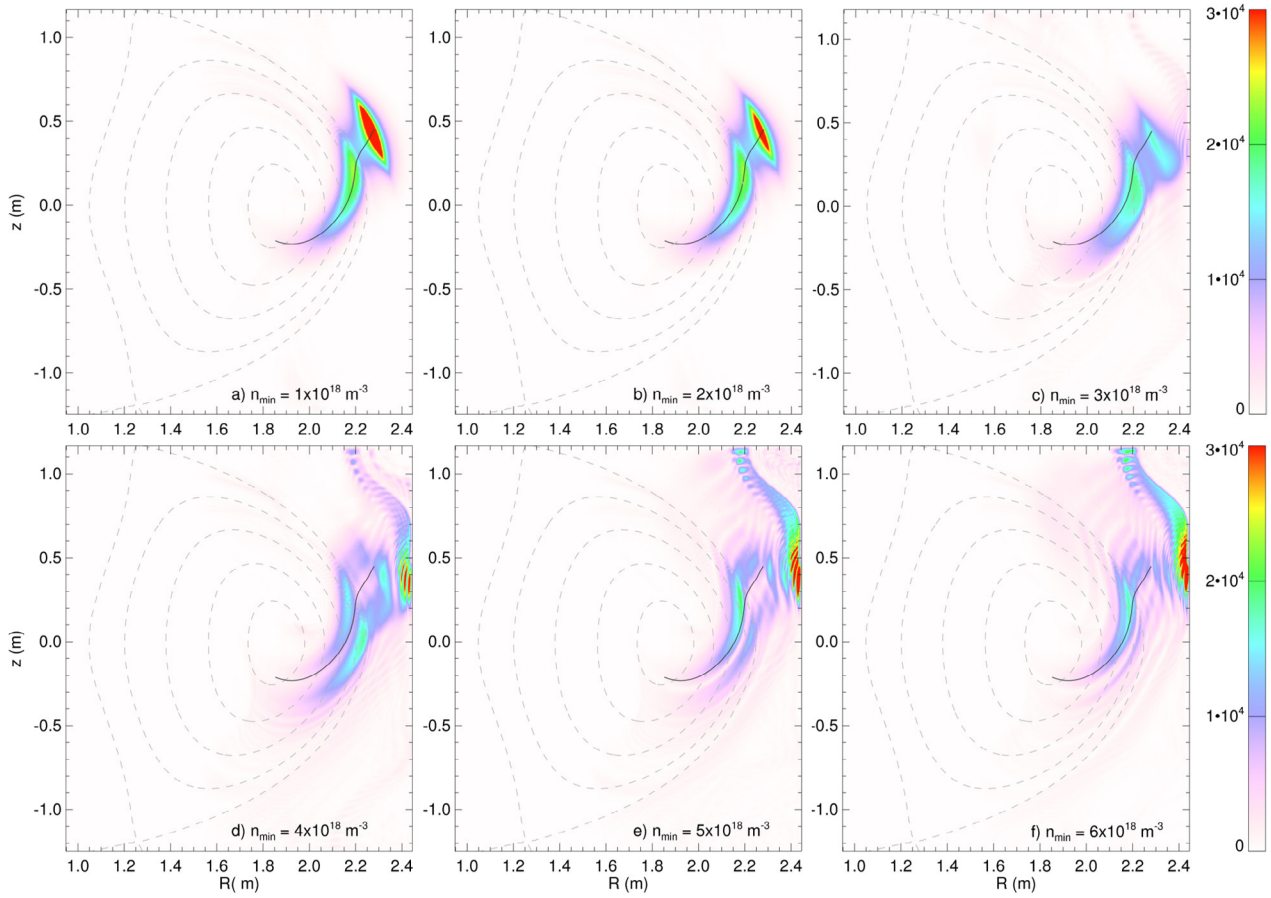

Figure 16. AORSA 2D simulations of the $|E|$ for DIII-D integrated scenario case including the SOL. GENRAY simulation is shown by the black solid line. (*a*) $n_{\min} = 1 \times 10^{18}$ m^{-3}. (*b*) $n_{\min} = 2 \times 10^{18}$ m^{-3}. (*c*) $n_{\min} = 3 \times 10^{18}$ m^{-3}. (*d*) $n_{\min} = 4 \times 10^{18}$ m^{-3}. (*e*) $n_{\min} = 5 \times 10^{18}$ m^{-3}. (*f*) $n_{\min} = 6 \times 10^{18}$ m^{-3}. $|E|$ is in units of V m^{-1}.

of the order of the slow wave perpendicular wavelengths (~few mm) are observed in these simulations. This may indicate that the slow wave is not an important factor in the SOL and is encouraging for interpreting the results of the AORSA 2D simulations where the grid resolution is not sufficient to resolve the slow wave in the SOL.

The helicon power lost to the SOL as a function of $n_{\min}$ is plotted in figure 15 in red squares for AORSA-1D. This power loss appears to be highest at low densities, with lower losses from $n_{\min}$ around 2–6 $\times$ 10^{18} m^{-3}. At low minimum SOL densities, such as $n_{\min} = 1 \times 10^{18}$ m^{-3} in figure 14(*a*)), the helicon wave is evanescent, so the antenna loading is lower and the SOL $|E|$ fields are higher. This leads to a higher lost power to the SOL.

AORSA 2D simulations are shown in figure 16 at various $n_{\min}$ for the DIII-D integrated scenario case at $n_{\|} = 4$. The GENRAY result including a SOL plasma is shown by the black curve. AORSA 2D $|E|$ path agrees with GENRAY from the antenna to the core plasma. At high $n_{\min}$, however, there appears to be another mode behind the antenna with significant $|E|$ that is not observed by the GENRAY model or the AORSA 1D model. The wave appears to be a helicon fast wave, as it has perpendicular wavelengths on the order of a few cm. The amplitude of this wave also grows with increasing $n_{\min}$. This high $|E|$ in the SOL reduces the power absorption and current drive in the core. The helicon power lost to the SOL as a function of $n_{\min}$ is shown in figure 15 in black circles. Similar to the AORSA 1D case, it can be seen that the power lost to the SOL increases at low densities. The increased SOL loss at low $n_{\min}$ is likely because antenna loading is low when the helicon wave is evanescent. However, there is certainly significant differences between the AORSA 1D and 2D simulations. Unlike the AORSA 1D simulations, the AORSA 2D simulations show higher losses. These losses are even higher at high SOL densities. The increased SOL loss at high $n_{\min}$ is correlated with high helicon $|E|$ fields in the SOL. For the given $\nu/\omega = .01$, the SOL loss for AORSA 2D can be a significant fraction (~10-20%) of the helicon wave absorption. It appears as if this additional mode in the SOL for the AORSA 2D cases is not observed in the AORSA 1D cases.

6. Discussion and conclusion

AORSA 1D, AORSA 2D, and GENRAY have been used to simulate the propagation and absorption of helicon waves for DIII-D and ITER integrated scenarios with and without SOL. For simulations without the SOL, AORSA 2D and GENRAY agree well for helicon wave electric field and power absorption profiles for DIII-D and ITER scenarios. It is therefore likely that GENRAY, which is a much less computationally intensive simulation, is sufficient to simulate core behavior of helicon waves.

Unlike the core behavior where there is good agreement between GENRAY and AORSA 2D, there are significant differences between GENRAY and AORSA when the SOL is included in the models. AORSA 2D predicts another mode that cannot be captured by the GENRAY model. This mode becomes much stronger as the SOL density is increased. The SOL power absorption trends are very similar to those that are observed in mid-harmonic and high-harmonic fast waves on DIII-D and NSTX in [54] where power loss to the SOL is observed at high and low SOL densities. There may therefore be an optimal SOL density to minimize the SOL power loss. For $\nu/\omega = .01$, the SOL loss at high density can be significant on the order of 10 to 20%. It will be important to confirm experimentally if high SOL densities affect helicon wave damping in the SOL. Tailoring the SOL density profile to optimize helicon current drive may reduce these SOL losses. Reducing the impact of SOL loss mechanisms (ν/ω in the simulation) will also reduce SOL losses. Further studies including both core and SOL in AORSA models, especially for high density reactor-relevant scenarios [55, 56], are needed to estimate core current drive efficiency and helicon wave SOL losses for a wider parameter scan. Including more realistic physical mechanisms for absorption in the SOL, rather than using ν/ω as a proxy for possible physical mechanisms, should also be considered.

It may therefore be worthwhile to study the helicon wave behavior in a reduced, full wave finite element model that uses fewer computational resources. While AORSA includes all the hot kinetic terms that can accurately calculate core power absorption and current drive, this may not be necessary to calculate SOL power loss in much colder plasmas. A model that includes only a portion of these hot terms may allow much faster calculation, while maintaining the essential features to accurately calculate trends in SOL power losses. Current AORSA simulations require too large computational resources for large parametric scans. A reduced model will allow for larger parametric scans that may lead to better physics understanding of helicon wave losses in the SOL and the formation of these SOL modes. In particular, a detailed study of the SOL profiles inputs to these simulations, such as varying ν, $n_{\min}$ or L, or by including more realistic density profiles or SOL loss mechanisms from experimental data, would be beneficial in understanding helicon losses to the SOL and allow for studying the parameters important for SOL losses and SOL mode formation. AORSA also only allows a rectangular boundary domain. Given that the |E| fields are significant at the boundaries of the simulation, the effects of a more realistic boundary condition that includes limiter and divertor geometries could be important in understanding these SOL modes. This finite element full wave model will be the focus of future work.

Acknowledgments

This work was supported by US Department of Energy, Office of Science, Office of Fusion Energy Sciences under contract numbers DE-AC05-00OR22725, DE-AC02-09CH11466, and DE-FC02-04ER54698. This research used resources of the National Energy Research Scientific Computing Center, a DOE Office of Science User Facility supported by the Office of Science of the U.S. Department of Energy under Contract No. DE-AC02-05CH11231.

ORCID iDs

C. Lau https://orcid.org/0000-0002-8576-5867

References

[1] Chan V.S. *et al* 2011 A fusion development facility on the critical path to fusion energy *Nucl. Fusion* **51** 083019
[2] Simonen T.C. *et al* 1988 Neutral-beam current-driven high-poloidal-beta operation of the DIII-D tokamak *Phys Rev. Lett.* **61** 1720
[3] Oikawa T. *et al* 2001 Reactor relevant current drive and heating by N-NBI on JT-60U *Nucl. Fusion* **41** 1575
[4] Murakami M. *et al* 2009 Off-axis neutral beam current drive for advanced scenario development in DIII-D *Nucl. Fusion* **49** 065031
[5] Geiger B. *et al* 2015 Fast-ion transport and neutral beam current drive in ASDEX upgrade *Nucl. Fusion* **55** 083001
[6] Surrey E. *et al* 2012 The influence of neutral beam optimization for DEMO on injector design *Fusion Eng. Des.* **87** 373–83
[7] Bernabei S. *et al* 1982 Lower-hybrid current drive in the PLT tokamak *Phys. Rev. Lett.* **49** 1255
[8] Hawkes N.C. *et al* 2001 Observation of zero current density in the core of JET discharges with lower hybrid heating and current drive *Phys. Rev. Lett.* **87** 115001
[9] Team T.S. *et al* 2003 Particle pinch with fully noninductive lower hybrid current drive in tore supra *Phys. Rev. Lett.* **90** 155002
[10] Bonoli P.T. *et al* 2008 Lower hybrid current drive experiments on Alcator C-Mod: comparison with theory and simulation *Phys. Plasmas* **15** 056117
[11] Majeski R. *et al* 1996 Mode conversion heating and current drive experiments in TFTR *Phys. Rev. Lett.* **76** 764
[12] Parisot A. *et al* 2007 Sawtooth period changes with mode conversion current drive on Alcator C-Mod *Plasma Phys. Control. Fusion* **49** 219
[13] Kazakov Y.O. *et al* 2014 Potential of ion cyclotron resonance frequency current drive via fast waves in DEMO *Plasma Phys. Control. Fusion* **57** 025014
[14] Brambilla M. and Bilato R. 2015 On radio frequency current drive in the ion cyclotron range of frequencies in DEMO and large ignited plasmas *Nucl. Fusion* **55** 023016
[15] Ono M. 1995 High harmonic fast waves in high beta plasmas *Phys. Plasmas* **2** 4075–82
[16] Petty C.C. *et al* 2001 Fast wave current drive at high ion cyclotron harmonics on DIII-D *Plasma Phys. Control. Fusion* **43** 1747
[17] Hosea J. *et al* 2008 High harmonic fast wave heating efficiency enhancement and current drive at longer wavelength on the National Spherical Torus Experiment *Phys. Plasmas* **15** 056104
[18] Matsuda K. 1989 Ray tracing study of the electron cyclotron current drive in DIII-D using 60 GHz *IEEE Trans. Plasma Sci.* **17** 6–11
[19] Isayama A. *et al* 2000 Complete stabilization of a tearing mode in steady state high-βp H-mode discharges by the first harmonic electron cyclotron heating/current drive on JT-60U *Plasma Phys. Control. Fusion* **42** L37

[20] Pietrzyk Z.A. *et al* 2001 Long-pulse improved central electron confinement in the TCV tokamak with electron cyclotron heating and current drive *Phys. Rev. Lett.* **86** 1530
[21] Petty C.C. *et al* 2002 Detailed measurements of the electron cyclotron current drive efficiency on DIII-D *Nucl. Fusion* **42** 1366
[22] Poli E. *et al* 2012 Electron-cyclotron-current-drive efficiency in DEMO plasmas *Nucl. Fusion* **53** 013011
[23] Vdovin V.L. 2013 Current generation by helicons and lower hybrid waves in modern tokamaks and reactors ITER and DEMO. Scenarios, modeling and antennae *Plasma Phys. Rep.* **39** 95–119
[24] Prater R. *et al* 2014 Application of very high harmonic fast waves for off-axis current drive in the DIII-D and FNSF-AT tokamaks *Nucl. Fusion* **54** 083024
[25] Smirnov A.P. *et al* 1994 *Bull. Am. Phys. Soc.* **39** 1626
[26] Ogawa T. *et al* 2001 Radiofrequency experiments in JFT-2M: demonstration of innovative applications of a travelling wave antenna *Nucl. Fusion* **41** 1767
[27] Pinsker R.I. *et al* 2016 Measurements of helicon antenna coupling in DIII-D *APS Meeting Abstracts (San Jose California, 31 October 2016)* (http://meetings.aps.org/Meeting/DPP16/Session/CO4.7)
[28] Wang S.J. *et al* 2017 Helicon wave coupling in KSTAR plasmas for off-axis current drive in high electron pressure plasmas *Nucl. Fusion* **57** 046010
[29] Bonoli P.T. and Ott E. 1982 Toroidal and scattering effects on lower-hybrid wave propagation *Phys. Fluids* **25** 359–75
[30] Bertelli N. *et al* 2013 The effects of the scattering by edge plasma density fluctuations on lower hybrid wave propagation *Plasma Phys. Control. Fusion* **55** 074003
[31] Wallace G.M. *et al* 2010 Absorption of lower hybrid waves in the scrape off layer of a diverted tokamak *Phys. Plasmas* **17** 082508
[32] Wallace G.M. *et al* 2011 Lower hybrid current drive at high density in Alcator C-Mod *Nucl. Fusion* **51** 083032
[33] Porkolab M. *et al* 1977 Observation of parametric instabilities in lower-hybrid radio-frequency heating of Tokamaks *Phys. Rev. Lett.* **38** 230
[34] Baek S.G. *et al* 2013 Measurements of ion cyclotron parametric decay of lower hybrid waves at the high-field side of Alcator C-Mod *Plasma Phys. Control. Fusion* **55** 052001
[35] Jaeger E.F., Berry L.A. and Batchelor D.B. 2000 Full-wave calculation of sheared poloidal flow driven by high-harmonic ion Bernstein waves in tokamak plasmas *Phys. Plasmas* **7** 3319–29
[36] Jaeger E.F., Berry L.A., D'Azevedo E., Batchelor D.B. and Carter M.D. 2001 All-orders spectral calculation of radio-frequency heating in two-dimensional toroidal plasmas *Phys. Plasmas* **8** 1573–83
[37] Budny R.V. *et al* 2012 Benchmarking ICRF full-wave solvers for ITER *Nucl. Fusion* **52** 023023
[38] Ehst D.A. and Karney C.F.F. 1991 Approximate formula for radiofrequency current drive efficiency with magnetic trapping *Nucl. Fusion* **31** 1933
[39] Phillips C.K. *et al* 2009 Spectral effects on fast wave core heating and current drive *Nucl. Fusion* **49** 075015
[40] Stix T.H. 1992 *Waves in Plasmas* (New York: AIP)
[41] Tooker J.F. *et al* 2017 Development of a high power helicon system for DIII-D *Fusion Eng. Des.* **123** 228–31
[42] Nagy A. *et al* 2017 A high power helicon antenna design for DIII-D *Fusion Sci. Technol.* **72** 623–7
[43] Park J.M. *et al* 2010 Experiment and modeling of ITER demonstration discharges in the DIII-D tokamak *23rd IAEA Fusion Energy Conf. (Daejon, Korea, 12 October 2010)* p 62 (www-pub.iaea.org/MTCD/Meetings/PDFplus/2010/cn180/cn180_BookOfAbstracts.pdf)
[44] Ferron J.R. *et al* 2013 Progress toward fully noninductive discharge operation in DIII-D using off-axis neutral beam injection *Phys. Plasmas* **20** 092504
[45] Murakami M. *et al* 2011 Integrated modelling of steady-state scenarios and heating and current drive mixes for ITER *Nucl. Fusion* **51** 103006
[46] Goldston R.J. *et al* 1981 New techniques for calculating heat and particle source rates due to neutral beam injection in axisymmetric tokamaks *J. Comput. Phys.* **43** 61–78
[47] Berry L.A., Jaeger E.F., Phillips C.K., Lau C.H., Bertelli N. and Green D.L. 2016 A generalized plasma dispersion function for electron damping in tokamak plasmas *Phys. Plasmas* **23** 102504
[48] Pinsker R.I. 2017 private communication
[49] Harvey R.W. and McCoy M.G. 1992 The CQL3D code *Proc. IAEA TCM on Advances in Simulation and Modeling of Thermonuclear Plasmas (Montreal, 5–18 June 1992)* USDOC/NTIS No. DE93002962, CQL3D Manual pp 489–526
[50] Wallace G.M. *et al* 2012 Lower hybrid current drive at high density in the multi-pass regime *Phys. Plasmas* **19** 062505
[51] Perkins R.J. *et al* 2012 High-harmonic fast-wave power flow along magnetic field lines in the scrape-off layer of NSTX *Phys. Rev. Lett.* **109** 045001
[52] Bertelli N. *et al* 2014 Full wave simulations of fast wave heating losses in the scrape-off layer of NSTX and NSTX-U *Nucl. Fusion* **54** 083004
[53] Lau C. *et al* 2015 Using AORSA to simulate helicon waves in DIII-D *AIP Conf. Proc.* ed R.I. Pinsker, vol 1689 (AIP Publishing) p 080011
[54] Bertelli N. *et al* 2015 Full wave simulations of fast wave efficiency and power losses in the scrape-off layer of tokamak plasmas in mid/high harmonic and minority heating regimes *Nucl. Fusion* **56** 016019
[55] Najmabadi F. *et al* 1997 Overview of the ARIES-RS reversed-shear tokamak power plant study *Fusion Eng. Des.* **38** 3–25
[56] LaBombard B. *et al* 2001 Particle transport in the scrape-off layer and its relationship to discharge density limit in Alcator C-Mod *Phys. Plasmas* **8** 2107–17